Title:

Numerical Simulation of Steam Electrolysis with a Solid Oxide Cell for Proper Evaluation of Cell Performances

Authors:

Yohei Tanaka [a, b,*], Michael Philipp Hoerlein [a], Günter Schiller [a]

Affiliations:

a) German Aerospace Center (DLR), Institute of Engineering Thermodynamics, Pfaffenwaldring 38-40, 70569 Stuttgart, Germany

b) Research Institute for Energy Conservation, National Institute of Advanced Industrial Science and Technology (AIST), Central 2, 1-1-1 Umezono, Tsukuba, 305-8568 Ibaraki, Japan

* *Corresponding author.* (present address) Yohei Tanaka, Ph.D, Central 2, 1-1-1 Umezono, 305-8568 Tsukuba, Ibaraki, Japan, tel +81-29-861-5091, fax +81-29-861-5805, E-mail address: tanaka-yo@aist.go.jp

Abstract:

A quasi-1D simulation model was developed to estimate total area-specific resistance for overvoltages (R_{tot}) and cell voltage by separating gas conversion impedance (GCI) from overall real-part impedance in high temperature steam electrolysis with a solid oxide cell (SOEC). GCI and R_{tot} for a square cell was estimated as 0.012-0.011 Ω cm^2 and 0.206-0.216 Ω cm^2, respectively, at J = 0.0-1.8 A cm^{-2}, 800°C, and relatively high flow rates. Even though GCI is small compared to R_{tot}, ignoring the GCI will result in higher simulation errors at J > 0.5 A cm^{-2}. Simulation results attained ±0.3 % or better precision against measured cell voltages at 750-850°C. Furthermore, case studies at 800°C revealed ±40 % local current density distribution in the cell at 1.0 A cm^{-2} and 82 % steam utilization. GCI was roughly inversely proportional to gas flow-rates and depended on steam utilization. Improvement of R_{tot} to 0.150 Ω cm^2 could attain more than 1.75 A cm^{-2} at 1.30 V.

Keywords: steam electrolysis; SOEC; hydrogen production; simulation model with equivalent circuit; gas conversion impedance

1 Introduction

As already issued in Germany, excess of intermittent renewable power from photovoltaic and wind power plants affects balance between supply and demand in power grids, causing instability of the grids [1−3]. Excess power is sometimes sold with negative electricity prices [2,3]. In Germany, renewable power plants are concentrated in northern parts, while much power is consumed in southern regions [3]. Thus, high-voltage transmission lines should be constructed and large-scaled power storage is necessary to stabilize the power-grid balance.

Hydrogen has attracted much attention as one of potential storage media for large scaled power [1]. There are several methods to produce hydrogen by electrolysis such as alkaline cells, polymer electrolyte cells, and solid oxide cells. Among the electrolysis methods, steam electrolysis at high temperatures with solid oxide cells (SOECs) has several advantages;

1. Thermodynamically, high temperature heat can reduce power demand in electrolysis, or ΔG [4]

2. This will lead to lower operating voltage and high energy efficiency. An operating voltage at an SOEC and a polymer electrolyte cell at 1.0 A cm^{-2} will be around 1.3 V and 2.0 V, respectively [5], though their voltages practically depend on system design and a targeted system efficiency.

3. Carbon dioxide as well as steam can be reduced to make syngas (H_2-CO) for synthetic fuels such as methane [6].

However, there are some issues in research and development of SOECs. Higher current density needs to be improve from the status quo, i.e. 0.2-1.0 A cm^{-2} and another issue is higher

degradation rate, that is generally 1-4 % per thousand hours [6-8] compared to solid oxide fuel cells (SOFCs) of 0.2-1 %/kh [9,10].

To develop an SOEC or its stack with better performance, evaluation of overvoltages derived from ohmic loss, activation processes, and gas diffusion in electrodes is important. Electrochemical impedance spectrometry (EIS) is often used to investigate these processes and to try separating each process and evaluate frequency-dependence and area specific resistance [11]. As an impedance spectrum of an SOFC is shown in Fig. 1, two semicircles or arches for higher and lower frequency processes would be often observed in EIS measurement in SOFCs. Considering analogy from SOFC, impedance spectra in SOEC may include a gas conversion impedance (GCI) [12,13]. GCI originates from gas composition change in gas channels due to altering current or voltage at lower frequencies with a characteristic frequency at typically 1.0 Hz or lower. For SOFCs, Primdahl et al. reported for a small electrode (0.50 cm^2) at a high fuel flow-rate (183 sccm cm^{-2}) [12] and Takano et al. for a practical-sized electrode (57 cm^2) at a reduced fuel flow-rate (3 sccm cm^{-2}) [13]. However, GCI has not been well discussed or quantified for SOEC in literature, except GCI was mentioned by Jensen et al. [14].

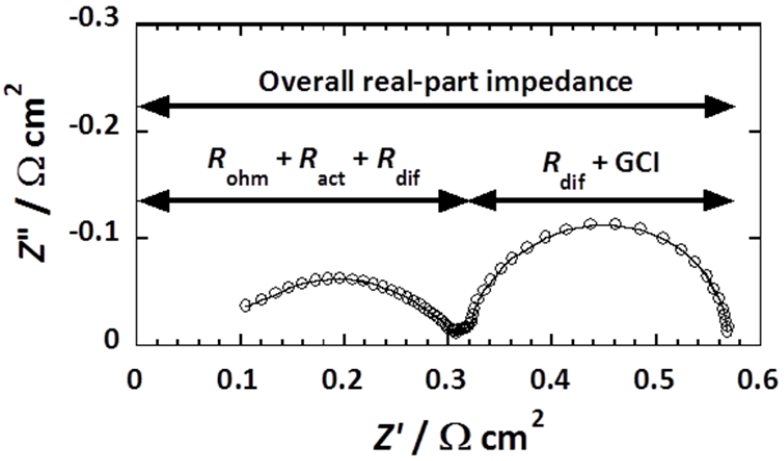

Fig. 1—An example of impedance spectra of a Ni-8YSZ-supported solid oxide fuel cell.

As depicted in Fig. 1, a confusing thing is that GCI could be merged with diffusion impedance at the similar lower frequencies in EIS measurements [15]. The diffusion impedance corresponds to concentration overvoltages derived from mass transport in electrodes which is driven by difference of gas concentration in each electrode between bulk and interface between one electrode and an electrolyte [16]. Diffusion impedance depends on electrode morphology in a cell and molecular size of gas species diffusing in the electrode. Therefore, the impedance differs from GCI. Primdahl et al. reported for the small SOFC, where gas composition change is very small, that GCI is proportional to an absolute temperature, inverse of gas flow-rate, and summation of inversed mole fraction of H_2 and H_2O ($1/\chi_{H2} + 1/\chi_{H2O}$) [12]. Takano et al. clarified by numerical simulation that the GCI characteristics can be applied in principle for the larger SOFC at reduced flow-rates where gas composition and current density changes drastically in the electrodes [13]. So, GCI estimation is more complicated at practical sized SOFCs at reduced flow-rates to increase fuel utilization to e.g. 80 %. From these points, GCI is just impedance influenced by gas-flow-rates, gas composition, temperature, and geometry of gas channels (height, porosity of current collectors and so on). Therefore, GCI should be considered apart from the overvoltages and corresponding area-specific resistances evaluated by EIS measurement or other means.

In this paper, to evaluate properly cell performance or area-specific resistance in high temperature electrolysis, numerical simulation methods were developed by considering GCI in SOEC. After GCI calculation, total area-specific resistance R_{tot} (Ω cm^2) at 750-850°C, which corresponds to sum of ohmic, activation, and diffusion overvoltages at a current density, was estimated with a quasi-1D simulation model coupled with experimental data using a semi-practical-sized square cell. We will discuss importance of considering GCI by comparing cell

voltages at different current-densities between simulation and experiment. In addition, case studies were carried out at 800°C to investigate effect of reduced gas flow-rate on cell performance and distribution of current density and other parameters in the cell and effect of R_{tot} on *V-J* curves.

Nomenclature

ac	alternating current
c	molar density (mol cm^{-3})
C	capacitance
CGO	gadolinium-doped ceria
D	binary diffusion coefficient (cm^2 s^{-1})
D^{eff}	effective binary diffusion coefficient (cm^2 s^{-1})
dc	direct current
E_{emf}	electromotive force (V)
EIS	electrochemical impedance spectroscopy
F	Faraday constant (96485 C mol^{-1})
f	flow rate (sccm)
GCI	gas conversion impedance (Ω cm^2)
ΔG	Gibbs free energy change
$\Delta G°_{H2O}$ (T)	Gibbs free energy change of hydrogen combustion at $p°$ and T (J mol^{-1})
h	gas channel height (cm)
I	current (A)
J	current density (A cm^{-2})
j_o	local current density (A cm^{-2})
LSCF	lanthanum strontium cobalt ferrite, $La_{0.58}Sr_{0.4}Co_{0.2}Fe_{0.8}O_{3-\delta}$
M	molecular weight (kg mol^{-1})
ORI	overall real-part impedance (Ω cm^2)
p	partial pressure (kPa)
$p°$	standard pressure (101.325 kPa)
R	gas constant (8.3145 J mol^{-1} K^{-1})
sccm	standard cubic centimeter per minute at 0°C and 101.325 kPa (cm^3 min^{-1})
T	temperature (K)
t	time (s)

U_{st}	steam utilization (%)
v	line velocity to x-direction (cm s^{-1})
V	voltage (V)
$\partial V/\partial J$	differential resistance (Ω cm^2)
Δx	length of a node to x-direction (cm)
8YSZ	8 mol% yttria-stabilized zirconia

Greek letters

ϵ_{po}	porosity (−)
ϵ	characteristic energy in the Lennard-Jones potential (J)
κ	Boltzmann constant (1.38067×10^{-23} J K^{-1})
σ	average collision diameter (Å)
τ	tortuosity (−)
χ	mole fraction (mol mol^{-1})
Ω_D	collision integral (−)

Subscripts

a	anode
act	activation
c	cathode
cell	cell
dif	diffusion
H_2	hydrogen
H_2O	water vapor
i	H_2, H_2O, O_2, or N_2
in	inlet
j	H_2, H_2O, O_2, or N_2
meas	measured
N_2	nitrogen
O_2	oxygen

ohm	ohmic
sim	simulated
tot	total

2 Simulation model

A simulation model was developed to calculate gas conversion impedance (GCI), voltage-current-density curve, and local distribution of mole fraction of gases, electromotive forces, and current densities in a single cell. In the simulation, GCI should be calculated first, followed by evaluation of total area-specific resistance R_{tot} which corresponds to total overvoltages. Then, those outputs were obtained after convergence. Details are explained in following subsections.

2.1 Geometry of a single cell unit

As shown in Fig. 2, a single cell unit used in experiments was modeled that consists of a cell (Forschungszentrum Jülich [17,18]), current collectors, and gas manifolds. The cell is composed of Ni-8YSZ/8YSZ/CGO/LSCF. This cell is supported by a 1 mm-thick Ni-8YSZ cathode (fuel electrode) on which 8YSZ electrolyte (10 μm), CGO interlayer (3 μm), and LSCF anode (air electrode, 30-40 μm) are sequentially deposited. Active electrode area is defined as one of 4 cm × 4 cm LSCF, 16 cm^2. To investigate local gas mole-fraction, electromotive force, and current density, x-direction was divided by 100, making a node size to x-direction, Δx = 0.040 cm.

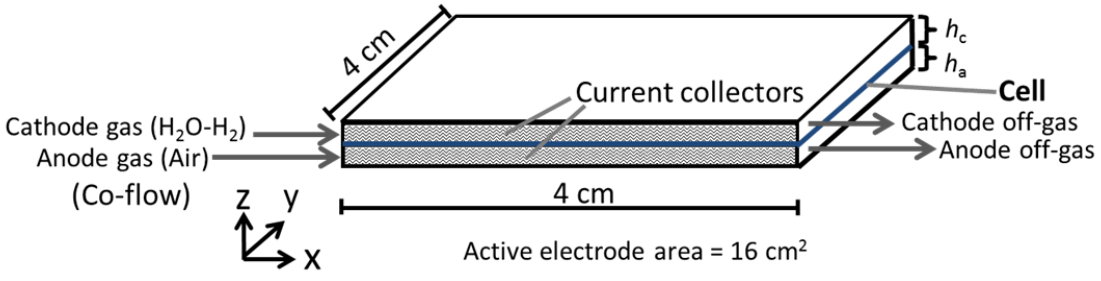

Fig. 2— Geometry of a single cell unit for experiment and numerical simulation.

Gas channel on cathode and anode is defined as a space between the electrode surface and the gas manifold surface for each electrode (4 cm × 4 cm × height h), which means not only space for a current collector but also grooves in the manifolds. Since the gas manifolds used in the experiment had complex grooves, averaged height of the gas channel for cathode and anode along z-direction is used as h_c = 0.174 cm and h_a = 0.174 cm, respectively. It was reported that size of GCI in SOFC is roughly proportional to channel height [13]. Most of the gas channels are filled with Ni and Pt current collectors for cathode and anode, respectively. The current collectors were made of plain-weave meshes. According to a porosity calculation equation for plain weave [19], an average porosity $\varepsilon_{po,c} = 0.945$ for the cathode gas channel and $\varepsilon_{po,a} = 0.953$ for the anode one was obtained respectively, considering the mesh sizes and wire diameters. Tortuosity τ for both electrodes is set at 1.05 for both gas channels derived from general relationship between ε_{po} and τ [20]. Both parameters influence gas diffusivity in the gas channels.

As exhibited in Fig. 2, cathode gas (82 % H_2O-H_2) and anode gas (imitated air, 20.95 % O_2-N_2) at a standard pressure p^o (101.325 kPa) are supplied in co-flow configuration to x-direction. The temperature of the cell, anode gas, and cathode gas was basically 800°C, otherwise noted. Cell voltage V_{cell} is defined as potential difference between the Pt current collector and the Ni current collector. In this paper, positive-value of current I, overall current density J, and local current density j_o means electrolysis mode.

2.2 Governing equations

To carry out numerical simulations at the standard gas pressure p^o or 101.325 kPa, following points were mainly assumed;

1. Gas flow to *x*-direction in a gas channel of both electrodes is homogeneous at any *y* position, so that quasi-1D simulation is valid considering the channel height *h* in *z*-direction.

2. Uniform temperature distribution in the cell including gases' temperatures

3. No gas leakage or mixture between anode and cathode sides

4. No electronic current through the 8YSZ electrolyte

5. Current efficiency is 1 to obey the Faraday's law that determines number of electrons transferred at electrochemical reactions in SOEC ($H_2O + 2e^- \rightarrow H_2 + O^{2-}$, $O^{2-} \rightarrow 0.5\ O_2 + 2e^-$)

6. Current collector for both electrodes has high electronic conductivity, so that V_{cell} is uniform at every local position in the cell

7. Gases behave as ideal gases

8. Pressure drop in anode and cathode can be ignored.

Following governing equations were used for simulation. Electromotive force E_{emf} was given by the Nernst's equation. Each partial pressure p_i was obtained from solving Eqs. 2-4 and 7.

$$E_{\mathrm{emf}} = -\frac{\Delta G^{\circ}_{\mathrm{H_2O}}(T)}{2F} + \frac{RT}{2F} ln \frac{\left(\frac{p_{\mathrm{H_2}}}{p^{\circ}}\right)\left(\frac{p_{\mathrm{O_2}}}{p^{\circ}}\right)^{0.5}}{\left(\frac{p_{\mathrm{H_2O}}}{p^{\circ}}\right)} \qquad (1)$$

Equations 2-4 express advection-diffusion equations to *x*-direction for H_2 and H_2O in cathode and O_2 in anode where the right-side terms mean molar rate per volume of H_2 and O_2 production or H_2O reduction due to the electrochemical reactions.

$$\frac{\partial c_{\mathrm{H_2}}}{\partial t} + \frac{\partial v_{\mathrm{c}}\, c_{\mathrm{H_2}}}{\partial x} - D^{\mathrm{eff}}_{\mathrm{H_2,H_2O}} \frac{\partial^2 c_{\mathrm{H_2}}}{\partial x^2} = \frac{j_{\mathrm{o}}}{2Fh_{\mathrm{c}}} \qquad (2)$$

$$\frac{\partial c_{\mathrm{H_2O}}}{\partial t} + \frac{\partial v_{\mathrm{c}}\, c_{\mathrm{H_2O}}}{\partial x} - D^{\mathrm{eff}}_{\mathrm{H_2,H_2O}} \frac{\partial^2 c_{\mathrm{H_2O}}}{\partial x^2} = -\frac{j_{\mathrm{o}}}{2Fh_{\mathrm{c}}} \qquad (3)$$

$$\frac{\partial c_{\mathrm{O_2}}}{\partial t} + \frac{\partial v_{a}\, c_{\mathrm{O_2}}}{\partial x} - D^{\mathrm{eff}}_{\mathrm{O_2,N_2}} \frac{\partial^2 c_{\mathrm{O_2}}}{\partial x^2} = \frac{j_{\mathrm{o}}}{4Fh_{\mathrm{a}}} \qquad (4)$$

where c_i is molar density for gas specie i, v_{c} and v_{a} is line velocity to x-direction of cathode gas and anode gas, respectively. The effective binary diffusion coefficients $D^{\mathrm{eff}}_{i,j}$ in Eq. 2-4 were given by Eq. 5 [21]

$$D^{\mathrm{eff}}_{i,j} = \frac{\epsilon_{po}}{\tau} D_{i,j} \qquad (5)$$

where ε_{po} and τ is porosity and tortuosity of a gas channel mainly governed by those of current collectors, respectively, for each electrode. Binary diffusion coefficients $D_{i,j}$ were obtained by the Chapman-Enskog theory [22,23]

$$D_{i,j} = 0.001858 \frac{\left[T^3\left(M_i + M_j\right)/M_i\, M_j\right]^{0.5}}{p^{\circ}\, {\sigma_{i,j}}^2\, \Omega_D} \qquad (6)$$

where T is an absolute temperature (K), $\sigma_{i,j}$ is average collision diameter (Å), Ω_{D} is a temperature-dependent collision integral (−), and M_i and M_j are molecular weight for gas species i and j. Ω_{D} was calculated as a function of the non-dimensional reduced temperature $T^* = T / (\varepsilon_{i,j} /\kappa)$ which is estimated from T and normalized characteristic energy $\varepsilon_{i,j}/\kappa = \sqrt{\frac{\varepsilon_i}{\kappa}\frac{\varepsilon_j}{\kappa}}$ in the Lennard–Jones potential for the binary system [23,24]. Detailed estimation way of Ω_{D} can be

seen elsewhere [23,25]. As shown in Table 1, these values were used for the advection-diffusion equations.

Table 1 Collision integral and binary diffusion coefficient

Temperature (°C)	Ω_D (-)		$D_{i,j}$ ($cm^2\ s^{-1}$)	
	H_2-H_2O	O_2-N_2	H_2-H_2O	O_2-N_2
750	0.8559	0.7228	7.04	1.66
800	0.8473	0.7173	7.64	1.80
850	0.8393	0.7121	8.26	1.94

Estimated from σ_{H_2,H_2O} = 2.734 Å, σ_{O_2,N_2} = 3.613 Å, $\varepsilon_{H_2,H_2O}/\kappa$ = 219.78 K, and $\varepsilon_{O_2,N_2}/\kappa$ = 87.28 K [24]

Using the equation of state, partial pressure for each gas specie was obtained as follows;

$$p_i = c_i R T \quad (7)$$

where i is H_2, H_2O, or O_2. Partial pressure of nitrogen was calculated by $p^o - p_{O_2}$. Continuity for cathode and anode sides was given as follows, respectively [13].

$$\frac{\partial v_c}{\partial x} = 0 \quad (8)$$

$$\frac{\partial v_a}{\partial x} = \frac{RT}{p^\circ}\frac{j_o}{4Fh_a} \quad (9)$$

As exhibited in Fig. 3, an equivalent circuit was presumed for every node that consists of R_{ohm}-$R_{act}C_{act}$-$R_{dif}C_{dif}$-E_{emf} where each area specific resistance R corresponds to ohmic, activation, and diffusion overvoltages, respectively. In this paper, only direct-current simulations were implemented, so that the capacitances size C is arbitrary. Local current density, j_o was obtained from Eq. 10. To evaluate distribution of the local current densities along x-direction, V_{cell} and total area-specific resistance R_{tot} (= R_{ohm} + R_{act} +R_{dif}) should be given. Therefore, each area-specific resistance is not necessary which is difficult to separate and obtain except by special techniques such as analysis of distribution of relaxation times (DRT) for impedance spectra [26,27].

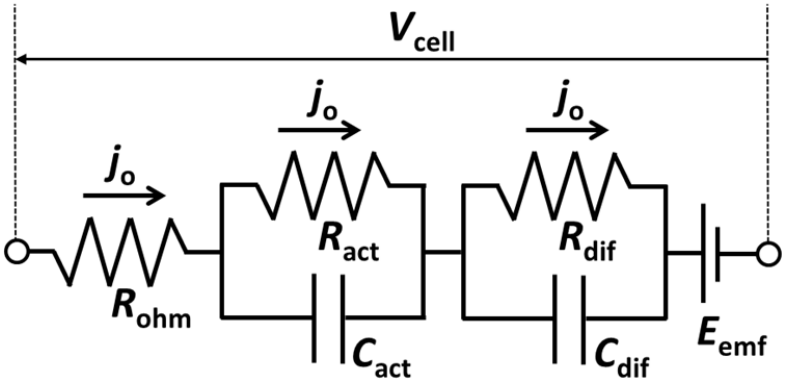

Fig. 3— Equivalent circuit for SOEC simulation

$$j_o = \frac{V_{cell} - E_{emf}}{R_{ohm}+R_{act}+R_{dif}} = \frac{V_{cell} - E_{emf}}{R_{tot}} \qquad (10)$$

An overall current I through the whole electrode is obtained by integrating j_o, which can be approximated as in Eq. 11.

$$I = \int_0^4 dy \int_0^4 j_o dx = 4 \int_0^4 j_o dx \approx 4 \sum j_{o,n} \Delta x \qquad (11)$$

where the $j_{o,n}$ represents a current density at n-th node in x-direction and Δx is length of a node (0.040 cm). Equation 12 represents relationship among I, steam flow-rate at cathode inlet, or $\chi_{H2O,in} f_c$ / (22414 × 60) (mol s^{-1}), and steam utilization U_{st} (%) according to the Faraday's law. The cathode-gas flow-rate f_c (sccm) is a volumetric flow-rate at 0°C and 101.325 kPa for ideal gas. Steam utilization means percentage of steam reacted in cathode by electrolysis and converted into hydrogen.

$$I = 2F \frac{\chi_{H_2O,in} f_c}{22414 \times 60} \frac{U_{st}}{100} \qquad (12)$$

2.3 Evaluation of GCI and R_{tot}

As mentioned in introduction and schematically shown in Fig. 1, real-part of impedance spectra will consist of impedances corresponding to not only ohmic, activation, and diffusion overvoltages but also gas conversion impedance (GCI). The diffusion impedance may be convoluted in the right lower-frequency arch. If GCI is properly estimated, the total area-specific resistance R_{tot} could be evaluated from the overall real-part impedance (ORI). In this paper, Eq. 13 was presumed.

$$R_{tot} = \text{ORI} - \text{GCI} \qquad (13)$$

This way of R_{tot} estimation is denoted as Method A. Overall real-part impedances were obtained at several current densities in impedance measurements described in section 3.

In addition, differential slope of voltage-current-density (*V-J)* curves, or $\partial V/\partial J$ should accord with ORI at ideal conditions. This is because 1. impedance is ratio between voltage and current, 2. real-part impedance reflects ability of a circuit to resist the flow of electrical current and 3. impedance measurements are carried out by superimposing small ac current on a dc current [11,28]. Therefore, R_{tot} could be also obtained by

$$R_{tot} = \partial V/\partial J - \mathrm{GCI} \qquad (14)$$

which is denoted as Method B for R_{tot} estimation. $\partial V/\partial J$ were calculated from experimentally obtained *V-J* curves and curve-fittings followed by differentiation.

Therefore, GCI should be estimated first with a value R_{tot} roughly guessed from EIS data. This rough use of R_{tot} as an initial value is acceptable since R_{tot} has only small impact on GCI as shown later. Thus, GCI was evaluated with R_{tot} = 0.200 Ω cm^2 for 800ºC guessed from excluding real-part of the lower-frequency arch from ORI at an experimental data at 1.0 A cm^{-2} (see Fig. 5 in section 4.1). Then, simulation of a *V-J* curve was carried out at R_{tot} = 0.200 Ω cm^2 and 0.0-1.8 A cm^{-2} to obtain $\partial V/\partial J$ by differentiation of the curve and GCI by transformed Eq. 14, or $\partial V/\partial J$ – 0.200 Ω cm^2.

Next, R_{tot} was finally estimated by Method A or Method B with the calculated GCI and experimentally obtained ORI or $\partial V/\partial J$ at several current densities *J*, respectively.

2.4 Solution method

First, gas composition and flow-rate of cathode and anode gases supplied to each electrode, a cell-and-gases temperature, R_{tot}, steam utilization U_{st}, and initial cell voltage (e.g. 0.900 V) were given.

Then, the advection-diffusion equations, or Eqs. 2-4 were solved by the explicit finite differential method in following boundary conditions (Eq. 15-18). It was presumed that there is no current at nodes for the left and right edges (x = 0-0.04 and 3.96-4.00 cm). Molar density at position x and time t is expressed as $c_i(x, t)$ for gas species i.

$$c_i(0,t) = \frac{p_{i,in}}{RT} = \frac{\chi_{i,\mathrm{in}}\, p^\circ}{RT} \quad (i = \mathrm{H_2, H_2O, O_2, N_2}) \qquad (15)$$

where $\chi_{i,\mathrm{in}}$ is mole fraction of gas specie i at gas inlets (x = 0).

For cathode,

$$c_{\mathrm{H2O}}(4,t) = \frac{\chi_{\mathrm{H2O,in}}\, p^\circ}{RT}\left(1 - \frac{U_{\mathrm{st}}}{100}\right) \qquad (16)$$

$$c_{\mathrm{H2}}(4,t) = \frac{p^\circ}{RT} - c_{\mathrm{H2O}}(4,t) \qquad (17)$$

For anode,

$$c_{\mathrm{O2}}(4,t) = \frac{\chi_{\mathrm{O2,in}}\, p^\circ}{RT}\left(1 + \frac{U_{\mathrm{ox}}}{100}\right) \qquad (18)$$

where U_{ox} (%) represents degree of O_2 evolution by electrolysis calculated from Eq. 19.

$$U_{\mathrm{ox}} = \frac{\chi_{\mathrm{H2O,in}}\, f_{\mathrm{c}}\, U_{\mathrm{st}}}{2\chi_{\mathrm{O2,in}}\, f_{\mathrm{a}}} \qquad (19)$$

Initial conditions for molar densities were given as

$$c_i(x, 0) = c_i(0, t) \quad (i = \mathrm{H_2}, \mathrm{H_2O}, \mathrm{O_2}, \mathrm{N_2}) \tag{20}$$

Iteration was continued with scanning V_{cell} until current I met one for a set steam utilization (Eq. 12) by ± 0.001 A and difference between $c_i(x, t)$ and $c_i(x, t + \Delta t)$ became less than 10^{-3} % where Δt is time step. As a simulation result, V_{cell}, I, J, local mole fraction χ_i, E_{emf}, and j_{o} were output.

3 Experimental

A Ni-8YSZ supported cell was used at 750-850°C to obtain *V-J* curves and electrochemical impedance spectra at several current densities. Impedance spectra were measured to evaluate overall real-part impedance (ORI) and R_{tot} by Method A as mentioned in section 2.3. On the other hand, *V-J* curves were used for evaluating $\partial V/\partial J$ and R_{tot} by Method B and also for comparing to V_{cell} simulation results.

As mentioned in section 2, the Ni-8YSZ/8YSZ/CGO/LSCF cell was obtained from Forschungszentrum Jülich, Germany [17,18]. The 1-mm thickness Ni-8YSZ support was produced by warm pressing using a so-called Coat-Mix material and pre-sintered at 1230°C. 5-10 μm NiO-8YSZ cathode-function-layer and 7-10 μm 8YSZ electrolyte were deposited on it by screen-printing and fired at 1400°C to obtain half-cells in the size of 5cm × 5 cm. The CGO layer was screen-printed on the electrolyte and sintered at 1300°C. Thickness of the CGO layer after sintering was 10-15 μm. Then, 4 cm × 4 cm LSCF anode ($La_{0.58}Sr_{0.4}$ $Co_{0.2}Fe_{0.8}O_{3-\delta}$) was prepared by screen-printing and finally sintered at 1050°C, giving 30-40 μm thickness. Active electrode area is defined as 16 cm^2 as in section 2.1.

As schematically exhibited in Fig. 2, a single cell unit was assembled with the cell, a Ni current collector for cathode, a Pt current collector for anode, and gas manifolds. Thermocouples were inserted at gas inlets and outlets. Gas sealing was implemented with gold rectangle-shaped ring for both electrodes [18]. During electrochemical measurements, temperature difference between inlet and outlet was about 2 K. This small temperature change suggests that hydrogen combustion due to gas leakage could be negligible and gas sealing would be almost perfect.

Cell testing started from heating up to 900°C at 3 K/min, followed by reduction procedure described elsewhere [29]. Then, cell temperature was decreased to 800°C where several *V-J* and EIS measurements were carried out at an ambient pressure. To investigate temperature-dependency of *V-J* curves, cell testing was also implemented at 750 and 850°C. For cathode, 82 % H_2O-H_2 was supplied at 2000 sccm via a H_2O-evaporator mixer (CEM 303A, Bronkhorst) using H_2 as a carrier gas controlled by a mass flow-controller (F-201C, Bronkhorst). Flow-rate of liquid water was controlled with a Coriolis mass-flow-controller (CORI-FLOW, Bronkhorst). Air was fed to the anode with a mass-flow-controller (F-201C, Bronkhorst).

In electrochemical measurements, an electronic-load instrument was used for *V-J* curve measurement at 0-24 A, or 0-1.5 A cm^{-2} (U_{st} = 0-10 %) or up to 1.3 V to prevent damage to the cell. On the other hand, electrochemical impedance spectra (EIS) were obtained using a potentiostat (PP240, Zahner) and an impedance spectrum analyzer (IM6, Zahner) at galvanostatic mode with 0.2 A amplitude from 40 kHz to 0.5 mHz. Impedance measurements were carried out at different current densities up to 1.0 A cm^{-2}.

4 Results and discussion

4.1 GCI estimation and V-J curve validation at 800°C

Gas conversion impedances (GCI) were estimated from *V-J* curve simulations assuming total area-specific resistance R_{tot} = 0.200 Ω cm^2 at 800°C. As shown in Fig. 4, GCI was estimated as 0.0121-0.0101 Ω cm^2 at J = 0.00-1.77 A cm^{-2}. These GCIs correspond to ca. a quarter of the lower frequency arch in the impedance spectra (see Fig. 5), while the residual 3/4 could be due to diffusion overvoltages since the Ni-8YSZ electrode was as thick as 1 mm. GCIs were also found to be only 4 % of the overall real-part impedances.

These GCIs are far lower than 0.5-1.0 Ω cm^2 reported by Takano et al. for a seal-less SOFC [13]. Though it is difficult to compare directly GCI at different conditions such as gas compositions and with/without gas seal for SOEC and SOFC, the GCI difference will be due to one in flow-rates per electrode-area considering from GCI principle that GCI is inversely proportional to gas flow-rate at a very small electrode [12]. We used the flow-rates per electrode area in this paper at 125 sccm cm^{-2} for fuel electrode and 189 sccm cm^{-2} for air electrode, while 3 sccm cm^{-2} and 15 sccm cm^{-2} were used in Takano's work [13], respectively. Since GCI is more affected by fuel flow-rate, 42-times higher fuel flow-rate in this paper was used than one in their work, which roughly agrees with the GCI difference by 42-100 times. Effect of flow-rates on GCI in the SOEC will be discussed in section 4.3.1.

As a result of sensitivity studies, it was confirmed that selection of R_{tot} will influence GCI calculation only by 0.0010 Ω cm^2 or smaller at 800°C and R_{tot} = 0.200-0.300 Ω cm^2. This will be because GCI in electrolysis originates from structure of the gas channels, porosity of the current collectors, temperature, and gas flow-rate instead of cell performance itself (R_{tot}). Thus, the GCI

estimation method can be reasonable and practical. The estimated GCIs will have at least ±0.0006 Ω cm^2 uncertainty at 95 % level of confidence, considering from uncertainty estimation type B assuming rectangular distribution. [30].

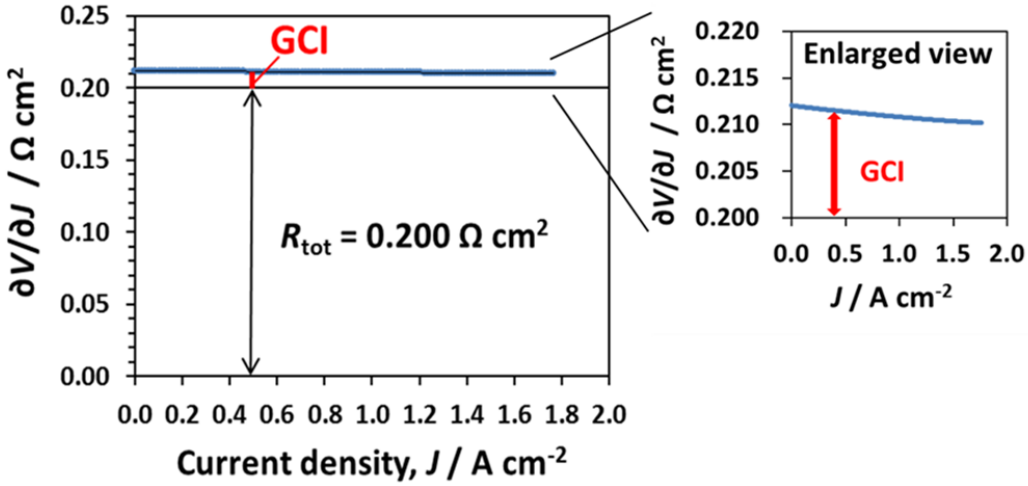

Fig. 4— GCI estimation from simulated $\partial V/\partial J$ at R_{tot} = 0.200 Ω cm^2 and 800°C. Simulation conditions: Cathode gas: 82 % H_2O-H_2 2000 sccm, anode gas: 20.95 % O_2-N_2 3000 sccm, U_{st} = 0-12 %.

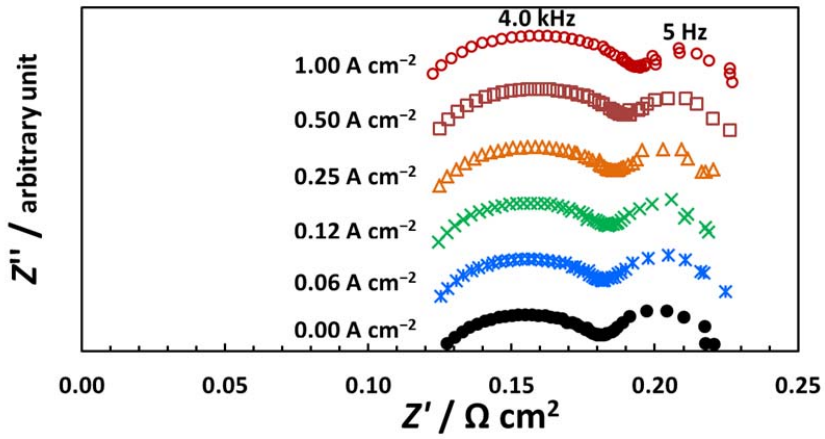

Fig. 5— Impedance spectra measured at 0.00-1.00 A cm^2 and 800°C. Experimental conditions: 82 % H_2O-H_2 2000 sccm, Air 3000 sccm, amplitude 0.2 A, frequency 40 kHz-0.5 Hz.

Then, cell voltages V_{cell} and *V-J* curves are simulated using calculated GCIs and experimentally obtained impedance spectra (Method A) and *V-J* curves (Method B). Figure 5 displays impedance spectra at 800°C at different current densities. From right edge positions of the real-part in each spectrum, overall real-part impedances (ORI) were determined. According to Eq. 13, subtraction of GCI from ORI gave R_{tot} (Method A) (see Table 2). On the other hand, by differential of the experimentally-obtained *V-J* curves as in Fig. 6, R_{tot} (Method B) was estimated from $\partial V/\partial J$ – GCI (Eq. 14). As exhibited in Table 2, R_{tot} was estimated as 0.2163 and 0.2151 Ω cm^2 at 1.00 A cm^{-2} from Methods A and B, respectively. R_{tot} difference between Methods A and B was ±0.008 Ω cm^2 at 0.00-1.00 A cm^{-2}.

In Table 2, simulation errors of V_{cell} against measured values for both methods were summarized. It was found that the Method A and the Method B can simulate cell voltages by ±0.21 % and ±0.12 % error, respectively. These small errors will correspond to ±0.009 Ω cm^2 and

$\pm 0.006\ \Omega\ cm^2$ errors in estimating R_{tot}, respectively. Therefore, assumed equations 13 and 14 for R_{tot} estimation are reasonable. The larger errors from the Method A may be due to somewhat scattered lower-frequency arch in the impedance measurements.

From the above, both methods can precisely predict cell voltages at high temperature steam electrolysis. And GCI and R_{tot} in SOEC will be well estimated by the simulation model.

Table 2 Estimation of GCI, R_{tot}, V_{cell}, and V_{cell} simulation error at 800°C

J (A cm^{-2})	GCI (Ω cm^2)	R_{tot} (Ω cm^2)			V_{cell} (V)			V_{cell} simulation error to measured value (%)	
		Method A	Method B	Difference	Method A	Method B	Measured	Method A	Method B
0.00	0.0122	0.2094	0.2062	0.0032	0.8716	0.8716	0.872	−0.05	−0.05
0.06	0.0121	0.2135	0.2112	0.0023	0.8855	0.8854	0.885	0.06	0.05
0.12	0.0120	0.2072	0.2143	-0.0071	0.8983	0.8992	0.899	−0.08	0.02
0.25	0.0118	0.2090	0.2166	-0.0076	0.9261	0.9281	0.927	−0.09	0.12
0.50	0.0115	0.2141	0.2143	-0.0002	0.9838	0.9838	0.984	−0.02	−0.02
1.00	0.0109	0.2163	0.2151	0.0012	1.0983	1.0973	1.096	0.21	0.12

Gas supply conditions were the same as in Fig. 6.

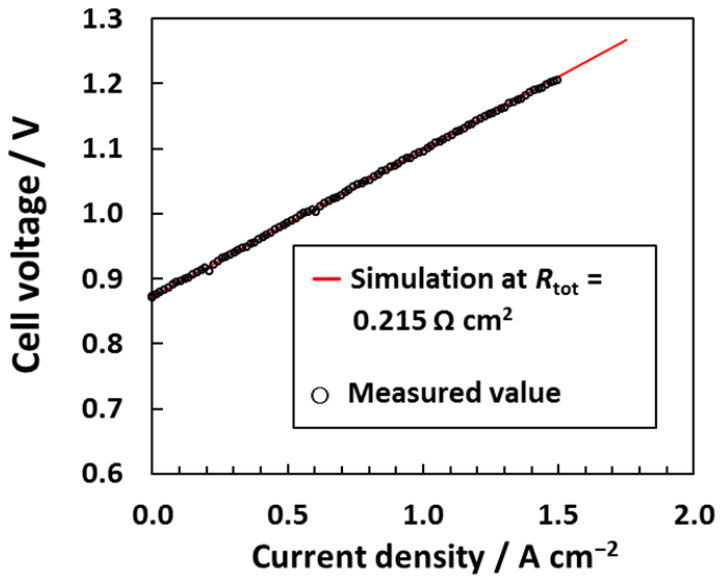

Fig. 6— Measured *V-J* curve and simulated one with a fixed R_{tot} (Method B) at 1.0 A cm^{-2} and 800°C. Cathode gas: 82 % H_2O-H_2, 2000 sccm, Anode gas: 20.95 % O_2-N_2, 3000 sccm in simulation and air, 3000 sccm in experiment.

Then, a *V-J* curve at 800°C was simulated using a fixed R_{tot} (Method B) at 1.00 A cm^{-2}, or 0.215 Ω cm^2 to simplify calculation process. This method was motivated by the small changes in R_{tot} at 0.00-1.50 A cm^{-2} (see Table 2), so that fixing R_{tot} could be allowed. As shown in Fig. 6, simulated curve agreed well with one measured at identical operating conditions. Error analyses clarified that simulation errors were ± 0.26 % to the measured values at 95 % level of confidence. Using a fixed R_{tot} for a higher current density was found to be a convenient way, though its precision will be somewhat worse than ±0.12 % in the point-to-point V_{cell} simulation by the Method B as in Table 2.

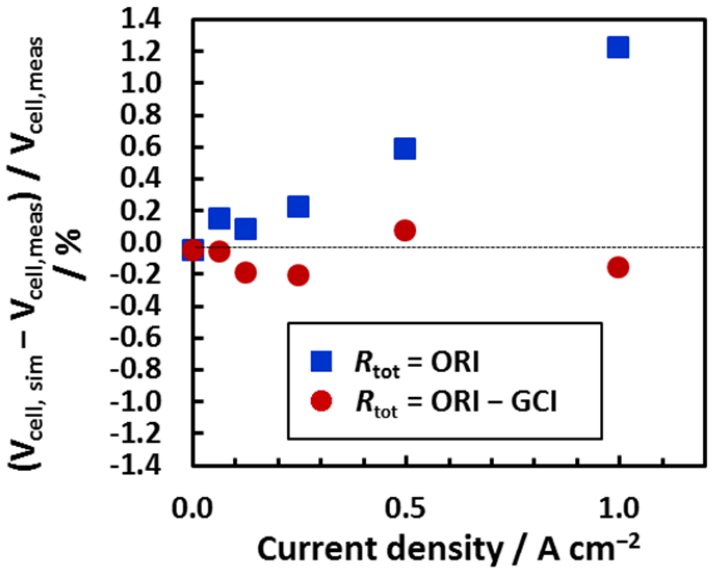

Fig. 7— Importance of GCI consideration for V_{cell} simulation precision at 800°C. Gas supply conditions were the same as in Fig. 6.

As mentioned above, simulated GCIs were about 4 % of overall real-part impedance, so that we investigated effect of GCI on V_{cell} simulation error, or $(V_{cell,sim} - V_{cell,meas})/ V_{cell,meas}$ to elucidate whether such small GCI can be ignored or not. As displayed in Fig. 7, it was clarified that the simulation errors could be bigger at higher current densities ($J \geq 0.5$ A cm^{-2}) when R_{tot} was given as ORI by omitting GCI. According to Eq. 10, cell voltages (V_{cell}) can be calculated by $V_{cell} = E_{emf} - R_{tot} j_o$, depending on R_{tot} and j_o, so that good precision of R_{tot} estimation will be required at higher densities J where local current density j_o tends to be large. Thus, even though GCI is small to overall real-part impedances or R_{tot} at the higher flow-rate conditions, it is important to consider and estimate GCI for precisely understanding cell performance and total area-specific resistance or total overvoltages.

It is sure that GCI may be ignored by increasing gas flow-rates further or decreasing active electrode area, since GCI at a practical-sized SOFC is almost inversely proportional to flow-rate [13]. However, this will not be beneficial for cell or stack testing with relatively large electrode area (> 10 cm^2) because supply at far larger flow-rates is required, resulting in difficulty in calibrating flow-rates and preheating gases. For the used cell case (16 cm^2), flow-rates should be ten times higher, or 20,000-30,000 sccm to reduce GCI to order of 0.001 Ω cm^2. Therefore, the simulation method considering GCI will be useful to understand total overvoltages and predict well-gas-sealed cell performance.

4.2 Temperature dependency validation

To evaluate validity of our simulation method at other cell temperatures, temperature-dependency of *V-J* curve was investigated with fixed R_{tot} for each temperature in the same manner as in section 4.1. R_{tot} = 0.364, 0.215, and 0.159 Ω cm^2 obtained from Method B at 0.50, 1.00, and 1.00 A cm^{-2} was used for simulations at 750, 800, and 850°C, respectively.

As displayed in Fig. 8, simulated *V-J* curves (solid lines) agreed well with measured ones (open symbols) also at 750°C and 850°C. Statistical analyses clarified that simulation errors to the measured V_{cell} were ± 0.42 % at 750°C, ± 0.26 % at 800°C, and ± 0.22 % at 850°C at 95 % level of confidence. The largest error at 750°C will be due to fluctuation of cell voltage in the experiment derived from intermittent unstable steam supply at 750ºC since two standard deviation of the measured voltage from a linear regression line was almost the same as the simulation error. If steam can be fed more stably, simulation error would be ± 0.3 % level.

Therefore, it was found that the simulation method fixing R_{tot} can precisely predict *V-J* curves at wide cell temperatures. Each R_{tot}, or total overvoltage and GCI could be evaluated precisely also at 750 and 850°C.

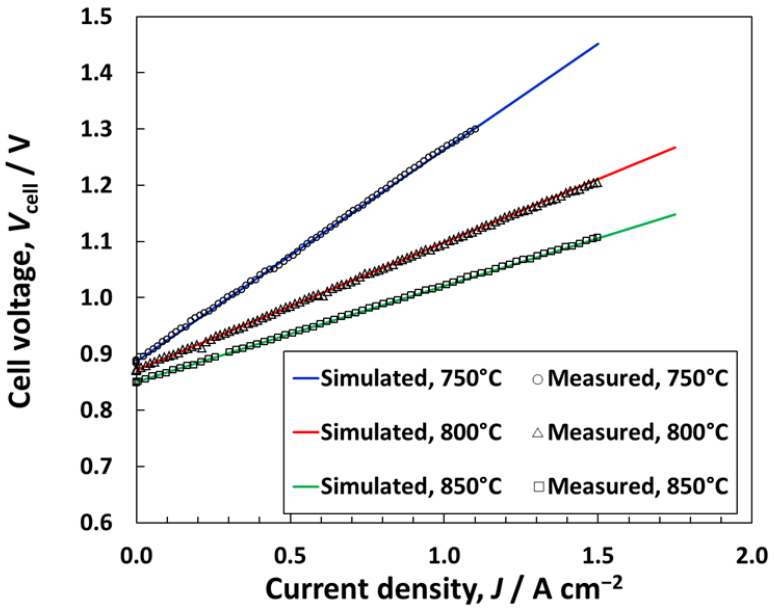

Fig. 8— Temperature dependency of *V-J* curve obtained by simulation and measurement at 750, 800, and 850°C with R_{tot} = 0.364, 0.215, and 0.159 Ω cm^2, respectively. Gas supply conditions were the same as in Fig. 6 .

4.3 Case studies at 800°C

Case studies were carried out to elucidate SOEC performance at more practical operating conditions, or reduced flow-rates. Simulations were implemented by the method with a fixed R_{tot} at 800°C, assuming R_{tot} is constant at every current density even if gas flow-rate and composition change. In addition, effect of R_{tot} on *V-J* curves was discussed.

4.3.1 Effect of reducing gas flow-rates for practical conditions

So far, gas flow-rates for cathode and anode was set as 2000 and 3000 sccm (hereafter, denoted as reference flow-rates) to the 16 cm^2 effective electrode area, respectively, in the simulations and experiments to suppress gas-composition change in the electrodes, leading to low steam utilizations such as 6.8-11.9 % at 1.0-1.75 A cm^{-2}. However, in practical operation of SOECs, reduced flow-rates are required to attain high steam utilization and higher energy efficiencies.

Effect of reducing flow-rate was investigated at 1/2, 1/4, 1/8, and 1/12 of the reference flow-rates at 800°C by simulation at R_{tot} = 0.215 Ω cm^2 in the same manner in section 4.2. The highest steam utilization was restricted at 99.4 % for the 1/12 flow-rate case, otherwise *V-J* curves were calculated at 0.00-1.75 A cm^{-2}. Figure 9 shows *V-J* curves for the different flow-rates. As flow-rate decreased, increase in cell voltages was observed. Since R_{tot} was common at those flow-rates, the V_{cell} differences were derived from ones in electromotive forces in the cell. Reduction of flow-rate at a current density leads to increase in H_2 mole fraction in cathode and O_2 fraction in anode, resulting in higher electromotive forces.

As emphasized in the 1/12 case (see Fig. 9), the *V-J* curve was more bent at lower and higher current densities and rather straight at mid-current-densities around 0.5-0.9 A cm^{-2}. As a result of GCI calculation for the case, as exhibited in Fig. 10, GCI against current density and steam utilization was found to be U-shaped in SOEC with 0.08-0.13 Ω cm^2. This agrees with the GCI shape for a 57 cm^2 SOFC where lower and higher fuel utilizations led to higher GCI [13]. The

shape in this paper was not perfectly symmetrical with its center at U_{st} = 50 % since the cathode-inlet steam mole fraction was 82 % instead of much higher one.

Validation of those *V*-*J* curves with experimental data will be desirable in future after a cell with larger electrodes is developed.

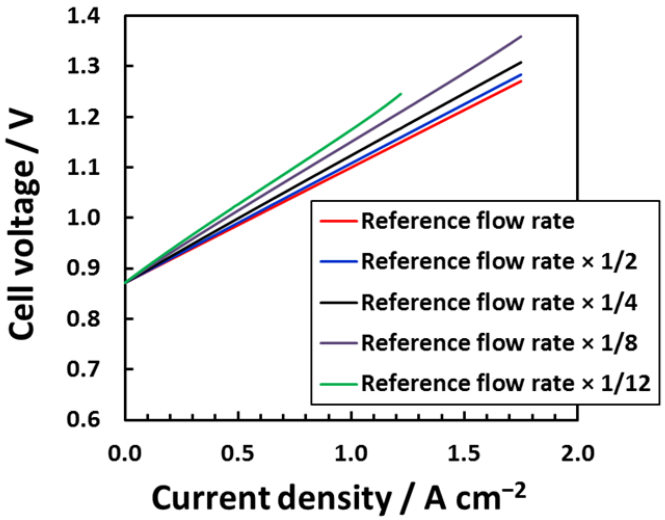

Fig. 9— Effect of reduced gas flow-rates on *V*-*J* curves at 800°C and R_{tot} = 0.215 Ω cm^2. Reference flow-rate: f_c = 2000 sccm, f_a = 3000 sccm. Gas compositions were the same as in Fig. 4.

Comparing to the 0.01 Ω cm^2-order GCIs at the reference flow-rates (section 4.1), GCI increased by one order of magnitude at 1/12 reduction of flow-rate (see Fig. 10). Table 3 shows GCI and specific GCI at 0.00 A cm^{-2} and 800°C for the reduced flow-rates. The specific GCI means a normalized GCI to one at the reference flow-rates. It was confirmed that GCIs in SOEC were roughly inversely proportional to the gas flow-rate at high temperature steam electrolysis, accounting for 10 % smaller from the principle. This result agrees with the GCI principle in solid oxide fuel cells with a small electrode area where gas composition change is small in the

electrodes [12]. The 10 % differences of specific GCIs from the principle may be because the modeled cell had a relatively large electrode area, 16 cm^2 and gas compositions change locally.

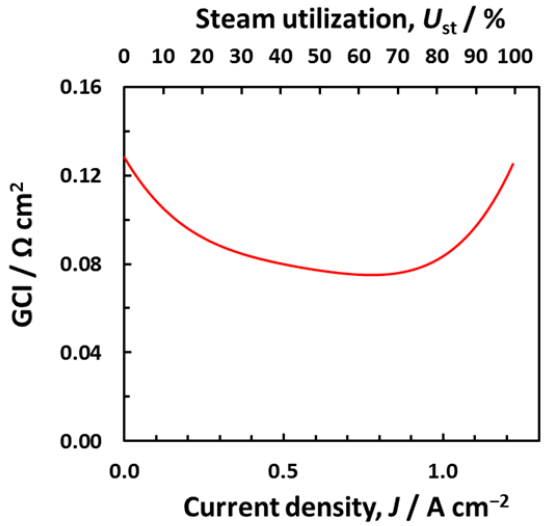

Fig. 10— GCI against current density and steam utilization at 1/12 of the reference flow-rate.

Gas supply conditions: f_c = 166.7 sccm, f_a = 250.0 sccm. Gas compositions were the same as in Fig. 4.

Table 3 Gas conversion impedance at 0.00 A cm^{-2} and 800°C for the reduced flow-rates

	Specific gas flow-rate for cathode and anode against reference one				
	Reference	1/2	1/4	1/8	1/12
GCI (Ω cm^2)	0.012	0.022	0.043	0.087	0.128
Specific GCI	1	1.8	3.6	7.3	10.8

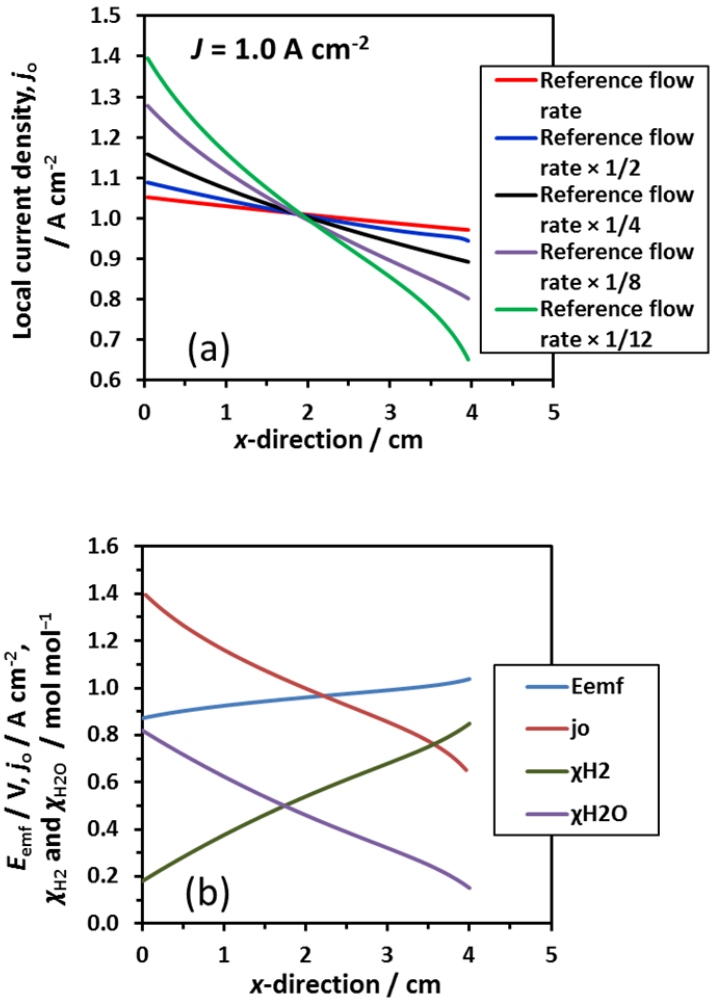

Fig. 11— (a) Local current density distribution at J = 1.00 A cm^{-2} and 800°C for reduced flow-rates and (b) local distribution of E_{emf}, j_o, χ_{H2}, and χ_{H2O} at 1/12 of the reference flow rate at 1.0 A cm^{-2} and U_{st} = 82 %. Gas composition of cathode and anode gases was the same as in Fig. 4.

Figure 11 (a) exhibits local current density (j_o) distributions in x-direction at reduced flow-rates. At the reference flow-rate, j_o distribution was almost flat, while decrease in flow-rate enhanced j_o at smaller x, or the gas inlet side and decreased j_o at the gas outlet side. This tendency was obvious at the 1/12 of the reference flow-rate case, giving ±40 % deviation of j_o to the

averaged 1.00 A cm^{-2} at 82 % steam utilization (U_{st}). Therefore, high steam utilization at practical SOEC operation will impose much higher current densities at the gas inlet in the case of co-flow configuration than averaged current density. Since it was reported that SOEC will be more deactivated at higher current densities than at lower ones [8], high steam utilization could locally deactivate cells and stacks at those higher current-density regions. When cells with a small electrode area are tested with higher flow-rates or lower steam utilization in long term, several current densities should be used, e.g. 40-50 % increased and decreased ones from a rated current density in practical operation.

Figure 11 (b) shows local distribution of electromotive force (E_{emf}), j_o, and H_2O-H_2 mole fractions (χ_{H2O}, χ_{H2}) in the cathode at the 1/12 of the reference flow-rates, 1.00 A cm^{-2} and U_{st} = 82 %. In proportion to j_o, steam was converted into H_2, leading to increase in E_{emf} at x= 4.0 cm (the gas outlet) from E_{emf} = 0.8715 V at the gas inlet which was almost equal to an open circuit voltage. Averaged E_{emf} along x-direction was estimated as 0.9573 V, which was by 58 mV higher than the E_{emf} at the gas inlet. Thus, this excess voltage was needed for electrolysis at U_{st} = 82 % in addition to the open-circuit voltage and the total overvoltages, 0.215 Ω cm^2 × 1.0 A cm^{-2} = 0.215 V for this case.

Distribution of current-density and gas composition will be measured in future after a larger cell is developed and these simulation results or the developed simulation method be validated.

4.3.2 Effect of total area-specific resistance

To assess targeted total area-specific resistances for cell development, effect of R_{tot} on *V-J* curves was investigated at 800°C with 1/8 of the reference flow-rates; 82 % H_2O-H_2 250 sccm,

20.95 % O_2-N_2 375 sccm. In the conditions, 1.5 A cm^{-2} corresponds to 81.5 % steam utilization. Figure 12 shows obtained *V-J* curves at the different R_{tot}. Decrease in R_{tot} to 0.150 and 0.100 Ω cm^2 from the reference 0.215 Ω cm^2 will suppress cell voltages down to 1.187 and 1.114 V at 1.5 A cm^{-2} and also 1.221 and 1.140 V at U_{st} = 90 % (1.66 A cm^{-2}), respectively.

Table 4 summarizes current densities at 1.300 V for the different R_{tot}. 1.300 V is near a thermo-neutral voltage for steam electrolysis at 800°C, or 1.287 V [31] that is calculated from lower heating value of H_2 combustion (248.3 kJ mol^{-1}) divided by 2 *F* assuming liquid H_2O is evaporated by heat exhausted from SOEC or other wasted heat. It is clarified that R_{tot} = 0.365 and 0.226 Ω cm^2 will be required to attain 1.00 and 1.50 A cm^{-2} at 1.300 V in the simulation conditions. When cell performance is improved to R_{tot}, which is equal or smaller than 0.150 Ω cm^2, current densities more than 1.75 A cm^{-2} can be expected.

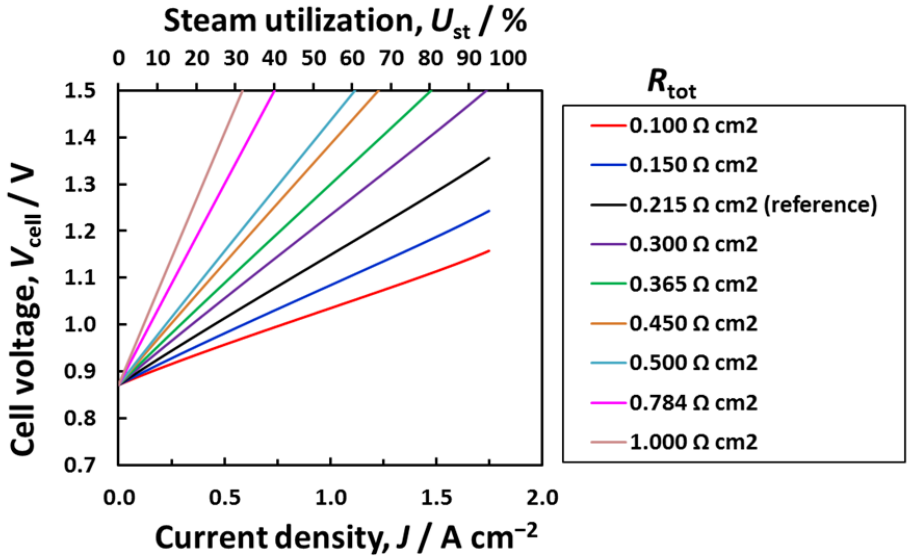

Fig. 12— Effect of R_{tot} on *V-J* curves at 800°C. Gas supply conditions: f_c = 250 sccm, f_a = 375 sccm, gas composition of cathode and anode gases was the same as in Fig. 6.

Table 4 Effect of R_{tot} on current density at 1.300 V and 800°C

R_{tot} (Ω cm^2)	0.100	0.150	0.226	0.215	0.300	0.365	0.450	0.500	0.784	1.000
Current density (A cm^{-2})	> 1.75	> 1.75	1.5	1.36	1.19	1.00	0.83	0.75	0.50	0.40

5 Conclusions

A quasi-1D simulation model was developed to interpret total area-specific resistance (R_{tot}) that accounts for total overvoltages in high temperature electrolysis of steam with a solid oxide cell (SOEC) and to discuss gas conversion impedance (GCI) in SOEC. The developed model was found to be a precise tool to estimate GCI, total area-specific resistance or total overvoltages, and *V*-*J* curve. Electrochemical impedance spectra in SOEC will include GCI. Detailed conclusions are summarized as follows.

(1) GCI for a square cell (16 cm^2) was estimated at 800°C and relatively large flow-rates, giving 0.012-0.010 Ω cm^2 at J = 0.0-1.8 A cm^{-2}. R_{tot} = 0.206-0.216 Ω cm^2 was estimated at J = 0.0-1.8 A cm^{-2} and 800°C accompanied with ±0.12-0.21 % errors in cell voltages against measured ones. Therefore, the developed model can precisely estimate GCI and R_{tot} for SOEC. Even though GCI is small compared to R_{tot}, ignoring the GCI will result in higher simulation errors especially at J > 0.5 A cm^{-2}.

(2) Another method fixing R_{tot} for each temperature can be easier than the point-to-point simulation above and attain ±0.3 %-level precision to measured cell voltages though it showed slightly higher errors. This method was found to be valid at different cell temperatures such as 750-850ºC.

(3) Case studies clarified that GCI in practical-sized SOEC (not button cell) is roughly inversely proportional to gas flow-rate and depends on steam utilization. Reducing flow-rates for practical SOEC operation will lead to large distribution of current density in a cell. Hence, degradation behavior will be worse at gas inlet side due to higher current densities. Furthermore, decrease of R_{tot} to 0.150 Ω cm^2 could attain more than 1.75 A cm^{-2} at 1.30 V and 800°C.

Acknowledgement

This work was carried out during the first author's stay at German Aerospace Center (DLR) in Stuttgart. He acknowledges support from his colleagues and administration staff. Part of the experiments was implemented in the course of Helmholtz Energy Alliance on electrochemical energy storage and conversion. The authors are grateful to Dr. Frank Tietz in Forschungszentrum Jülich, Germany for providing the cell and its information.

References

[1] Ehteshami SMM, Chan SH. The role of hydrogen and fuel cells to store renewable energy in the future energy network – potentials and challenges. Energy Policy, 73 (2014) 103–109. DOI: 10.1016/j.enpol.2014.04.046

[2] Nicolosi M. Wind power integration and power system flexibility–An empirical analysis of extreme events in Germany under the new negative price regime. Energy Policy, 38 (2010) 7257–7268. DOI:10.1016/j.enpol.2010.08.002

[3] Paraschiv F, Erni D, Pietsch R. The impact of renewable energies on EEX day-ahead electricity prices. Energy Policy, 73 (2014) 196–210. DOI: 10.1016/j.enpol.2014.05.004

[4] Udagawa J, Aguiar P, Brandon NP. Hydrogen production through steam electrolysis: Model-based steady state performance of a cathode-supported intermediate temperature solid oxide electrolysis cell. J. Power Sources, 166 (2007) 127–136. DOI: 10.1016/j.jpowsour.2006.12.081

[5] Ferrero D, Lanzini A, Santarelli M, Leone P. A comparative assessment on hydrogen production from low- and high-temperature electrolysis. Int. J. Hydrogen Energy, 38 (2013) 3523−3536. DOI: 10.1016/j.ijhydene.2013.01.065

[6] O'Brien JE, McKellar MG, Harvego EA, Stoots CM. High-temperature electrolysis for large-scale hydrogen and syngas production from nuclear energy – summary of system simulation and economic analyses. Int. J. Hydrogen Energy, 35 (2010) 4808–4819. DOI: 10.1016/j.ijhydene.2009.09.009

[7] Zhang X, O'Brien JE, O'Brien RC, Hartvigsen JJ, Tao G, Housley GK. Improved durability of SOEC stacks for high temperature electrolysis. Int. J. Hydrogen Energy, 38 (2013) 20−28. DOI: 10.1016/j.ijhydene.2012.09.176

[8] Moçoteguy P, Brisse A. A review and comprehensive analysis of degradation mechanisms of solid oxide electrolysis cells. Int. J. Hydrogen Energy, 38 (2013) 15887−15902. DOI: 10.1016/j.ijhydene.2013.09.045

[9] Yokokawa H. Report of Five-Year NEDO Project on Durability/Reliability of SOFC Stacks. ECS Transactions, 57 (1) (2013) 299-308. DOI:10.1149/05701.0299ecst

[10] Bucheli O, Bertoldi M, Modena S, Ravagni AV. Development and Manufacturing of SOFC-Based Products at SOFCpower SpA. ECS Transactions, 57 (1) (2013) 81-88. DOI: 10.1149/05701.0081ecst

[11] Huang QA, Hui R, Wang B, Zhang J. A review of AC impedance modeling and validation in SOFC diagnosis. Electrochimica Acta, 52 (2007) 8144–8164. DOI: 10.1016/j.electacta.2007.05.071

[12] Primdahl S, Mogensen M. Gas Conversion Impedance: A Test Geometry Effect in Characterization of Solid Oxide Fuel Cell Anodes. J. Electrochem. Soc., 145(7) (1998) 2431−2438. DOI: 10.1149/1.1838654

[13] Takano K, Nagata S, Nozaki K, Monma A, Kato T, Kaga Y, Negishi A, kato K, Inagaki T, Yoshida H, Hosoi K, Hoshino K, Akbay T, Akikusa J. Numerical simulation of a disk-type SOFC for impedance analysis under power generation. J. Power Sources, 132 (2004) 42−51. DOI: 10.1016/j.jpowsour.2004.01.038

[14] Jensen SH, Sun X, Ebbesen SD, Knibbe R, Mogensen M. Hydrogen and synthetic fuel production using pressurized solid oxide electrolysis cells. Int. J. Hydrogen Energy, 35 (2010) 9544−9549. DOI: 10.1016/j.ijhydene.2010.06.065

[15] Primdahl S, Mogensen M. Gas Diffusion Impedance in Characterization of Solid Oxide Fuel Cell Anodes. J. Electrochem. Soc. 146(8) (1999) 2827−2833. DOI: 10.1149/1.1392015

[16] Fuel Cell Handbook (7th edition), EG&G Technical Services, Inc., (2004) 2-4−2-16.

[17] Schafbauer W, Schulze-Küppers F, Baumann S, Meulenberg WA, Menzler NH, Buchkremer HP, Stöver D. Tape Casting as a Multi Purpose Shaping Technology for Different Applications in Energy Issues. Mater. Sci. Forum 706-709 (2012) 1035-1040. DOI: 10.4028/www.scientific.net/MSF.706-709.1035

[18] Hoerlein MP, Schiller G, Tietz F. Development and Characterisation of Solid Oxide Electrolyser Cells (SOEC). 11th European SOFC and SOE Forum 2014 Proceedings, European Fuel Cell Forum (2014) B1316 1-6.

[19] Zhao Z, Peles Y, Jensen MK. Properties of plain weave metallic wire mesh screens. Inter. J. Heat Mass Transfer, 57 (2013) 690–697. DOI: 10.1016/j.ijheatmasstransfer.2012.10.055

[20] Matyka M, Khalili A, Koza Z. Tortuosity-porosity relation in porous media flow. Phys. Rev., E 78 (2008) 026306. DOI: 10.1103/PhysRevE.78.026306

[21] Litster S, Epting WK, Wargo WA, Kalidindi SR, Kumbur EC, Morphological Analyses of Polymer Electrolyte Fuel Cell Electrodes with Nano-Scale Computed Tomography Imaging. Fuel Cell, 13(5) (2013) 935–945. DOI: 10.1002/fuce.201300008.

[22] Hayes RE, Mmbaga JP, Introduction to Chemical Reactor Analysis. Second Edition, CRC Press, (2012) 373.

[23] Revankar ST, Majumdar P. Fuel Cells: Principles, Design, and Analysis. CRC Press, (2014) 257-264.

[24] Sinha AP, De P. Mass Transfer: Principles and Operations. PHI Learning Pvt. Ltd., (2012) 30-36.

[25] Shimada T, Momma A, Takano K, Kato T. Numerical analysis of electrical power generation and internal reforming characteristics in seal-less disk-type solid oxide fuel cells. J. Power Sources 187 (2009) 8-18. DOI: 10.1016/j.jpowsour.2008.10.125

[26] Schichlein H., Müller AC, Voigts M, Krügel A, Ivers-Tiffée E. Deconvolution of electrochemical impedance spectra for the identification of electrode reaction mechanisms in solid oxide fuel cells. J. Appl. Electrochem., 32 (2002) 875–882.

[27] Kornely M, Neumann A, Menzler NH, Leonide A, Weber A, Ivers-Tiffée E. Degradation of anode supported cell (ASC) performance by Cr-poisoning. J. Power Sources 196 (2011) 7203– 7208. DOI: 10.1016/j.jpowsour.2010.10.033

[28] Lvovich VF. Impedance Spectroscopy: Applications to Electrochemical and Dielectric Phenomena. John Wiley & Sons, (2012) 1-5.

[29] Haanappel VAC, Smith MJ. A review of standardising SOFC measurement and quality assurance at FZJ. J. Power Sources, 171 (2007) 169–178. DOI: 10.1016/j.jpowsour.2006.12.029

[30] ISO/IEC Guide 98-3:1995. Guide to the Expression of Uncertainty in Measurement (GUM). International Organization for Standardization, (2008) 11-15.

[31] Bierschenk DM, Wilson JR, Miller E, Dutton E, Barnett SA. A Proposed Method for High Efficiency Electrical Energy Storage Using Solid Oxide Cells. ECS Trans., 35 (1) (2011) 2969-2978. DOI: 10.1149/1.3570297